Al$_2$O$_3$:Cr^{3+} Nanotubes Synthesized via Homogenization Precipitation Followed by Heat Treatment

Baochang Cheng,* Shengchun Qu, Huiying Zhou, and Zhanguo Wang

Key Laboratory of Semiconductor Materials Science, Institute of Semiconductors, Chinese Academy of Sciences, P.O. Box 912, Beijing 100083, People's Republic of China

Received: April 11, 2006; In Final Form: June 12, 2006

Cr^{3+}-doped NH$_4$Al(OH)$_2$CO$_3$ nanotubes, templated by surfactant assemblies, were successfully synthesized via the homogenization precipitation method, and various crystallographic phase Al$_2$O$_3$:Cr^{3+} nanotubes were also obtained by postannealing at different temperatures. The characteristic R$_1$, R$_2$ doublet line transitions of ruby can be observed in the high crystalline α-Al$_2$O$_3$ nanotubes calcined at temperatures higher than 1200 °C. The results also indicate that the formation mechanism of the tubular nanostructures should result from the self-rolling action of layered compound NH$_4$Al(OH)$_2$CO$_3$ under the assistance of the surfactant soft-template. The convenient synthetic procedure, excellent reproducibility, clean reactions, high yield, and fine quality of products in this work make the present route attractive and significant. Aluminum oxide nanotubes with high specific surface area could be used as fabricating nanosized optical devices doped with different elements and stable catalyst supports of metal clusters.

1. Introduction

Over the past decades, there has been a rapidly increasing interest in one-dimensional (1D) nanostructures because of their novel properties, derived from their unique structural one-dimensionality and quantum size confinement effects in two dimensions, as well as their wide variety of potential applications as catalysts, field-emission cathodes, magnetic storage and recording media, gas sensors, solar cells, and electronic components.[1−3] Special attention has been paid to the preparation of nanotubes of metallic oxides due to their anticipated exciting properties and promising applications in electronics, mechanics, physics, and chemistry arising from shape-specific and quantum-size effect.[4,5] These researches have concentrated on compounds characterized by layered or anisotropic crystal structures, for example, graphite, boron nitride, and metal disulfides. Recent reports indicate that some geometrically closed, concentric nanotubes from nonlayered structural materials, such as GaN, Si, SiO$_2$, et al., have been synthesized by the choice of proper experimental conditions.[5−15] There is some unique property for nanotubular structures, e.g., they may act as a physical shield for the inserted biomolecules and provide advantages for biomolecule delivery, especially there is a more novel application for the fluorescent nanotubes.[15] Therefore, it will be of significance for the fabrication of technologically and practically important doping and polynary complex nanotubes through a simple synthetic procedure.

Al$_2$O$_3$ plays a key role in many technologies due to its remarkable physical properties, such as a high melting point, hydrophobicity, high elastic modulus, high optical transparency, high refractive index of about 1.76 at 632.8 nm wavelength, thermal and chemical stability, low surface acidity, and fine optical and dielectric characteristics.[16−19] Al$_2$O$_3$ can act as a tunneling barrier for novel magnetic sensors and for organic transistors because of its large band gap (8 eV).[20] Al$_2$O$_3$ coatings could also potentially serve as high temperature-resistant

coatings, which have various applications in space and energy production technologies.[21] It is well-known that γ-Al$_2$O$_3$ is an extremely important form of the known alumina crystalline phases, widely applied to a catalyst and a catalyst support of transition element clusters in the automotive and petroleum industries, and α-Al$_2$O$_3$ doped with transition metal Cr^{3+} and Ti^{3+} ions is the most important phase for laser hosts, possessing excellent emitting properties.[22−25] Al$_2$O$_3$ exhibits more than 15 distinct crystallographic phases, and it can undergo a variety of transitions until the most-stable corundum structure (α-Al$_2$O$_3$), in which all the cations are in a six-coordinate environment, forms at high temperature. Thus, alumina will be an attractive building block for functional nanostructures. In the past few years, considerable effort has been directed toward the preparation of various morphologic α-Al$_2$O$_3$ nanostructures such as nanowires,[26,27] nanobelts,[28] nanofibers,[29,30] and whiskers.[31] Amorphous Al$_2$O$_3$ nanotubes also can be obtained through various approaches.[32] However, α-Al$_2$O$_3$ is rarely prepared,[36,37] especially doped Al$_2$O$_3$ polymorphs. Therefore, an exploration of new synthetic routes is needed. Herein, Cr^{3+}-doped NH$_4$Al(OH)$_2$CO$_3$ nanotubes, templated by surfactant assemblies, were successfully synthesized by a novel homogeneous precipitation method with urea, and Al$_2$O$_3$:Cr^{3+} nanotubes with different crystalline phases were also obtained by postannealing treatment at different temperatures. The synthetic technique of doping and polynary complex nanostructures through the simple chemical route can be contributed to the absolutely uniform distribution of cations in nanohosts by the liquid phase, and furthermore, the simple synthetic procedure, excellent reproducibility, high yield, and fine quality of products make the present route attractive and significant.

2. Experimental Section

2.1. Material Synthesis. The Cr-doped NH$_4$Al(OH)$_2$CO$_3$ nanotubes were first synthesized by means of the homogeneous precipitation method with the assistance of surfactant. Al(NO$_3$)$_3$, Cr(NO$_3$)$_3$, hexadecyltrimethylammonium bromide [(C$_{16}$H$_{33}$)N$^+$-
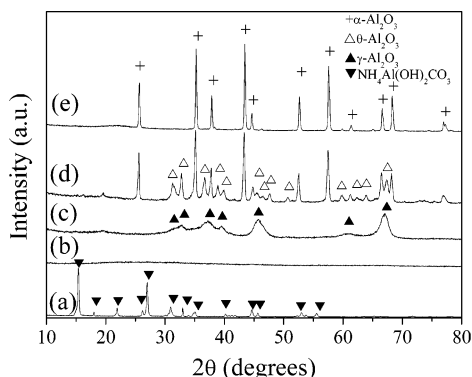
Figure 1. XRD patterns of the Cr^{3+}-doped samples: (a) as-grown from solution and (b–e) postannealed at 600, 900, 1100, and 1200 °C, respectively.

$(CH_3)_3 \cdot Br^-$, CTAB], urea, and water were mixed at a molar ratio of 1:0.02:1:5:400 and simultaneously stirred to obtain a transparent solution. The solution was put into a Teflon-coated stainless steel autoclave, and then heated at 125 °C and kept at that temperature under autogenous pressure. After 15 h, the autoclave was cooled to room temperature naturally. The resulting slurry was collected by filtration, washed several times with distilled water and absolute ethanol, and then dried in air at 100 °C for 10 h. After this the resulting powders were subjected to thermolysis in the range of 600 and 1200 °C for 3 h in a static air atmosphere to obtain various crystallographic Cr^{3+}-Al_2O_3 nanotubes.

2.2. Characterization. The products were characterized by X-ray diffraction (XRD; Phillips X'Pert PRO with Cu Kα radiation), field emission scanning electron microscopy (FES-EM; JEOL JSM-6700F), transmission electron microscopy (TEM; Hitach H800, at 200 kV), and high-resolution TEM (HRTEM; JEOL JEM-2010, at 200 kV). BET surface area, calculated by the Brunauer–Emmett–Teller (BET) equation using the data in a P/P_0 range between 0.05 and 0.2, was determined from the corresponding nitrogen adsorption isotherm, at low temperature (77 K), with a gas sorption analyzer (COULTER, Omnisorp-100CX). The room temperature pho-toluminescence (PL) and photoluminescence excitation (PLE) spectra of the products were measured by a fluorescence spectrophotometer (Edinburgh FLS920) with a 450 W xenon lamp and by a micro-PL system of a Confocal Laser Micro-Raman spectrometer (LABRAM-HR, France JY Company) with the 514.5 nm line of an Ar^+ ion laser (output power amounts to about 4 mW and the laser beam was focused to the minimum spot size of about 5 μm on the specimen surface by an objective lens), respectively, as an excitation light source.

3. Results and Discussion

3.1. Morphology and Structure. The loose powders with a very slight reddish tint, obtained from aqueous solution, were heat treated at various temperatures for 3 h in a static air atmosphere. The structural analysis by XRD for the samples, obtained from solution and postannealed at the different temperatures, is presented in Figure 1a–e. As can be seen from Figure 1a, the clearly distinguishable sharp peaks of the product, prepared by the soft chemical method, are indicative of high crystallinity. All of the diffraction peaks can be neatly indexed to end-centered orthorhombic Ammonium Aluminum Hydroxide Carbonate [$NH_4Al(OH)_2CO_3$] phase (JCPDS No. 76-1923). Under the assistance of CTAB surfactant, the well-crystallized $NH_4Al(OH)_2CO_3$ phase was formed during the hydrothermal treatment process. After thermal decomposition of NH_4Al-
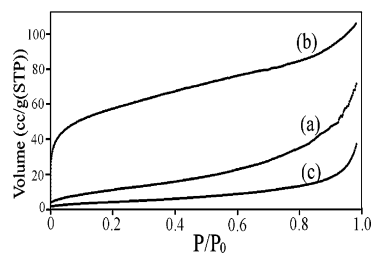

Figure 2. Adsorption isotherms of nitrogen at 77 K for the samples: (a) as-prepared by the soft chemical method and (b and c) postannealed at 900 and 1200 °C, respectively.
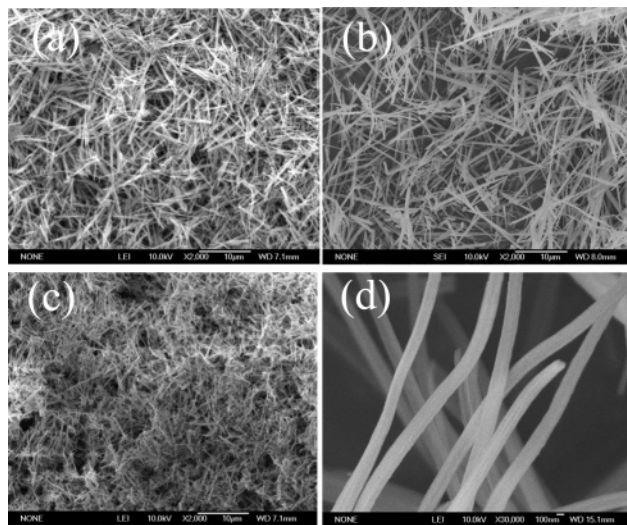

Figure 3. FE-SEM images of the products: (a) obtained from aqueous solution; (b) postheated at 600 °C for 3 h; and (c and d) postheated at 1200 °C for 3 h.

$(OH)_2CO_3$ at 600 °C, amorphous Al_2O_3 is observed (Figure 1b). Subsequent treatment at 900 °C shows a pure cubic γ-Al_2O_3 (JCPDS No. 02-1420) with very broad diffraction peaks, indicating a small crystal size. At the sintering temperature of 1100 °C, the monoclinic θ-Al_2O_3 and hexagonal α-Al_2O_3 phases are simultaneously formed. As the calcination temperature is raised above 1200 °C, the single hexagonal α-Al_2O_3 phase (JPCDS No. 46-1212) is finally formed with good crystalliza-tion. No other phase is found, because the foreign element, such as carbon and hydrogen from the surfactant, can be oxidized easily at high temperature. Additionally, the concentration of Cr^{3+} is very low, and furthermore, Cr^{3+} ions can incorporate into Al_2O_3 lattice and form substituted solid solution. From the analysis results of XRD, the phase evolution of the doping samples can be schematically described as follows with increas-ing calcination temperature: $NH_4Al(OH)_2CO_3 \rightarrow$ amorphous $Al_2O_3 \rightarrow$ γ-$Al_2O_3 \rightarrow$ θ-$Al_2O_3 \rightarrow$ α-Al_2O_3. The crystal size first decreases and then increases with increasing calcination tem-perature. This is very consistent with the analysis result of the Brunauer–Emmett–Teller (BET) surface area as shown in Figure 2. The as-synthesized Cr^{3+}-doped $NH_4Al(OH)_2CO_3$ nanostructures exhibit a surface area of 43 m^2/g. After the precursors were annealed at 900 °C for 3 h, surface area ascends rapidly up to 340 m^2/g, originating from the thermal decomposi-tion of the Cr^{3+}-doped $NH_4Al(OH)_2CO_3$ phase and the formation of a smaller sized γ-Al_2O_3 phase inside the tube wall (Figure 4c). High specific surface area would make γ-Al_2O_3 extremely advantageous for practical application as catalysts and catalyst support materials. As the samples are converted into the α-Al_2O_3 phase after 3 h of firing at 1200 °C, however, it is found to be noticeably lower, but still large (16 m^2/g), indicative of an
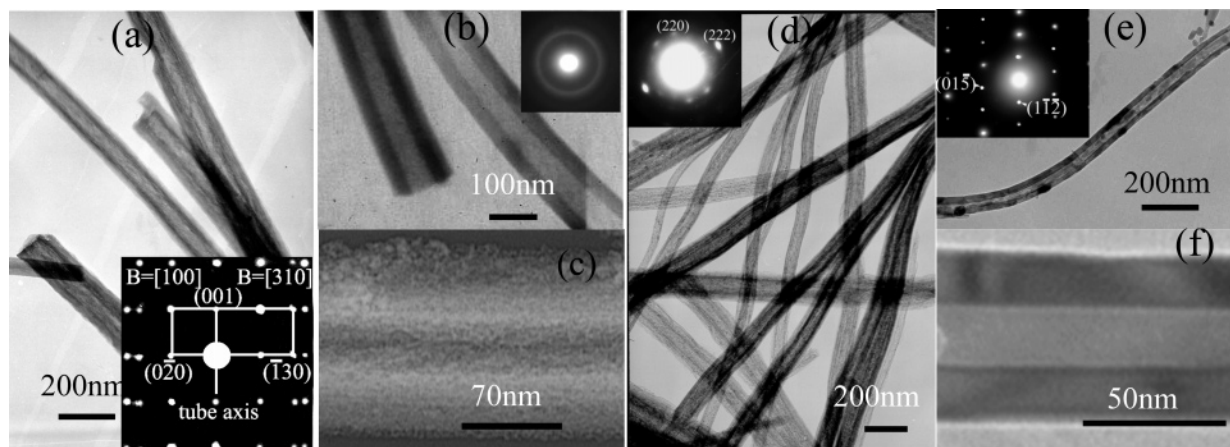
Synthesis of Al$_2$O$_3$:Cr^{3+} Nanotubes

J. Phys. Chem. B, Vol. 110, No. 32, 2006 **15751**

Figure 4. Representative TEM images and corresponding SAED patterns of the successive processes occurring during the growth of Al$_2$O$_3$:Cr^{3+} nanotubes annealed at the different reaction stages: (a) as-synthesized NH$_4$Al(OH)$_2$CO$_3$:Cr^{3+} nanotubes from aqueous solution at 125 °C, corresponding SAED can be indexed to an end-centered orthorhombic structure and exhibit a superposition of two specific patterns belonging to [310] and [100] zones, and the tube axis is depicted as shown along the [001] direction; (b and c) at 600 °C; (d) at 900 °C; and (e and f) at 1200 °C. Insets in panels b, d, and e are corresponding SAED patterns that can be indexed to amorphous, cubic, and hexagonal Al$_2$O$_3$ structures, respectively.

increase in crystallinity. It can also be found that Cr can hamper abnormal grain growth of Al$_2$O$_3$ during sintering, making the microstructure fine, and the phase transition occurs at higher temperature in contrast with the undoped samples. With the increase of the calcination temperature, the color of the samples changes gradually. After heat treatment at 600 °C, they become green due to the presence of the small amount of Cr^{3+} clusters in amorphous alumina. At 900 °C, they become yellow. The samples eventually become pink after sintering at 1200 °C, indicating that Cr^{3+} ions have entirely incorporated into Al$_2$O$_3$ hosts, uniformly substitute for Al^{3+} sites, and form isolated single ion states.

The general morphology of the samples was examined with field emission scanning electron microscopy (FE-SEM) and transmission electron microscopy (TEM). FE-SEM images of the products, obtained from aqueous solution and postcalcined at different temperatures, are shown in Figure 3, respectively. As can be seen from the FE-SEM images, all of the samples consist of relatively uniform 1D nanostructures with diameters of about 100−200 nm and lengths ranging from several to tens of micrometers. The nanofibers remain free-standing, remarkably with no sign of aggregation through the whole crystallization process; however, a slight average decrease in diameter is already noticeable. The shrinkage of the diameter is attributed to the pyrolysis of the precursor and the increase of the crystallinity. Figure 4 shows TEM images of the samples annealed at various temperatures. From the results of TEM observations, quantities of tubular nanostructures can be clearly seen, with a high contrast between the edge and the central part of the tube. The nanotube outer diameters are estimated to be around 100−200 nm, and the wall thickness is distinguished readily by the darker contrast to be about 40−60 nm. Furthermore, the tubular structures are not destroyed after firing at different temperatures, and the coalescence and the crystallinity of nanoparticles only occur within tube walls. Unfortunately, the lattice stripe image of the Cr^{3+}-doped NH$_4$Al(OH)$_2$CO$_3$ nanotubes cannot be effectively explored because they are extremely sensitive to electron beam irradiation during the TEM examinations. It is observed that under intensive electron beam irradiation, NH$_4$Al(OH)$_2$CO$_3$ nanotubes rapidly bend and transform into amorphous structures, derived from their decomposition. The SAED pattern, taken with the incident beam perpendicular to the surface of the nanotube at very weak current density and inset in Figure 4a, can be indexed to a superposition

of two sets of specific patterns belonging to [310] and [100] zone axes, which should come from the top (basal plane) and lateral regions of tube wall due to a curled structure. The tube axis is perpendicular to the row of {001} reflections. After 3 h of annealing at 600 °C, the tube wall becomes tinier nanoparticles (Figure 4b,c), and moreover, the corresponding selected area electron diffraction (SAED) pattern (the inset in Figure 4b) takes on an only diffusive ring, indicative of an amorphous nature. From the SAED pattern for the samples annealed at 900 °C (the inset in Figure 4d), the two brighter dot-rings, corresponding to the (222) and (220) diffractions of γ-Al$_2$O$_3$, can be seen. The result implies that the γ-Al$_2$O$_3$ tubular walls are obviously orientated. For the samples calcined at 1200 °C, however, the SAED pattern (the inset in Figure 4e), taken with the electron beam along the [751] zone axis, displays a clearly spotted pattern and can be indexed to the reflections of the α-Al$_2$O$_3$ phase, indicative of good crystalline quality and structural uniformity after postannealing treatment at higher temperature. These results demonstrate that with the increase of the calcination temperature, the Cr^{3+}-doped NH$_4$Al(OH)$_2$CO$_3$ nanotubes first convert into amorphous alumina nanotubes consisting of tinier nanoparticles, and finally, orientationally crystallize to quasisingle crystalline nanotubes.

Figure 5 depicts the high-resolution TEM (HRTEM) images of the sidewall portion of typical Al$_2$O$_3$:Cr^{3+} nanotubes, postannealed at 1100 and 1200 °C, and provides further insight into the structure details of Al$_2$O$_3$:Cr^{3+} nanotubes. From the image of the sample calcined at 1100 °C (Figure 5a), it can be clearly seen that there exists a great deal of distortion and disorder in the lattice, indicating poor crystallinity. For the image of the samples calcined at 1200 °C (Figure 5b), however, the nearly perfect lattice fringes illustrate that Cr^{3+} ions have absolutely incorporated into the Al$_2$O$_3$ host, uniformly occupied Al^{3+} cation sites, and formed substitutional solid solutions with a high crystallinity. The distinct interplanar spacing of the tube wall is measured to be about 0.39 nm, which is in good agreement with the ideal values of the {101} planes of the α-Al$_2$O$_3$ bulk crystal. The corresponding fast Fourier transform analysis (the upper inset in Figure 5b) indicates that the incident beam is along the [21$\bar{2}$] direction.

3.2. Optical Properties. The room temperature photoluminescence (PL) and photoluminescence excitation (PLE) spectra of the sample calcined at 1200 °C, using a 450 W xenon lamp as a light source, are acquired and shown in Figure 6a. As seen
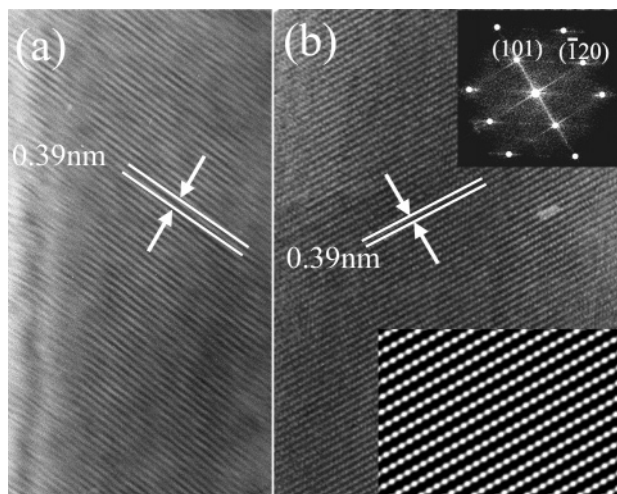
Figure 5. HRTEM images of the rim part of the Al$_2$O$_3$:Cr^{3+} nanotube wall with clearly resolved lattice fringe of (101) planes ($d = 0.39$ nm) (a and b) postcalcined at 1100 and 1200 °C, respectively. The upper and lower insets in panel b correspond to Fourier transform and invert Fourier transform analyses of the image, respectively.

from the PLE spectrum monitored at 694 nm, two strong broad absorption bands with peak positions at around 409 and 567 nm, corresponding to spin-allowed $^4A_2(^4F) \rightarrow {}^4T_1(^4P)$ and $^4A_2$-$(^4F) \rightarrow {}^4T_2(^4F)$ transitions of Cr^{3+} ions on the octahedral sites of α-Al$_2$O$_3$, and a weak sharp peak at 462 nm, corresponding to the transition of $^4A_2(^4F) \rightarrow {}^2T_2(^2G)$, are observed. From the PL spectrum, well-known narrow R lines at 494 nm, ascribed to the $^2E \rightarrow {}^4A_2$ transition of isolated single Cr^{3+} ions which substitute for Al^{3+} ions on the octahedral sites of the spinel block, are observed. This indicates that the nanostructured ruby is formed, and furthermore, the intensity is excited more with use of the 567 nm yellow light than with the 409 nm ultraviolet light. To investigate further the properties of the stimulated emission, the PL spectra for the samples, postcalcined at various temperatures, were also measured by a micro-PL system of a Confocal Laser Micro-Raman spectrometer, using the 514.5 nm line of an Ar$^+$ ion laser with a power density of about 20 kW/cm2 as an excitation light source, and the results are presented in Figure 6b. For the sample calcined above 1200 °C, the PL spectrum shows a significant difference from those calcined at relatively low temperatures in PL properties. At high photogeneration density, the stimulated emission very easily takes place and characteristic emission of the R line is split into two clearly resolvable sharp peaks centered at 694.3 (R$_1$) and 692.9 (R$_2$)

nm with a full width at half-maximum of less than 0.7 nm; moreover, their intensities exhibit a superlinear increase with the pump power. With further increasing calcination temperature, in addition, the intensity of the R lines is also enhanced remarkably, indicative of higher crystallinity with the octahedral crystal field. The two weak sharp peaks also appear at 705 and 701.5 nm, called N$_1$ and N$_2$ lines, which arise respectively from second and fourth nearest-neighbor exchange-coupled pairs of Cr^{3+} ions due to comparatively high Cr^{3+} concentration.[38] The PL spectra for the samples calcined at a relatively low temperature exhibit an asymmetric broad-band emission in the range of 650−900 nm, attributed to the cluster centers of Cr^{3+} ions.[39] Under the low-temperature calcination condition, the as-prepared powders first changed into the amorphous state with tinier nanoparticles, which might lead to some Cr contact and form clusters. In addition, a large quantity of hanging bonds and defects also exist in this nanosized imperfect crystal, which further lead to the broadening and weakening of the emission band related to Cr^{3+}. With increasing calcination temperature, the broad band blue shifs and becomes narrow, which indicates the luminescent centers transfer from cluster states to pair states and finally to isolated single ion states, originating in the uniform substitution of Cr^{3+} on the Al^{3+} cationic sites in the octahedral crystal field at higher annealing temperature. These results demonstrate that the line shape of the Cr^{3+} emission in Al$_2$O$_3$ depends intensively on the crystal structure and Cr^{3+} ion coupling states. The typical fluorescence characteristic of the ruby crystal confirms that Cr^{3+} as a guest ion has been well introduced within the crystal lattice of the Al$_2$O$_3$ nanotubular wall without the formation of phase segregation of the Cr^{3+} ions in the lattice as the samples were postcalcined at temperature above 1200 °C.

3.3. Formation Mechanism of Nanotubes. NH$_4$Al(OH)$_2$CO$_3$ with a space group *Cmcm*, whose three-dimensional sketch of the crystal structure is shown in Figure 7a, exhibits a layer-shape structure. The structural elements in crystals mainly consist of corner- and edge-sharing AlO$_6$ octahedra, which first form long chains parallel to the *c*-axis and then form layered structures parallel to {110} facets. Layers are connected together by hydrogen bonds in neighboring planes. For this layered anisotropic crystal structure, similar to those of graphite, bismuth, WS$_2$, and MoS$_2$ compounds, it is very easy to form tube-like nanostructures under proper experimental conditions. The key is how to overcome the interactions between layers and provide the driving force for the rolling process.[41−45] At the initial stage of the nucleation and incubation, the behavior
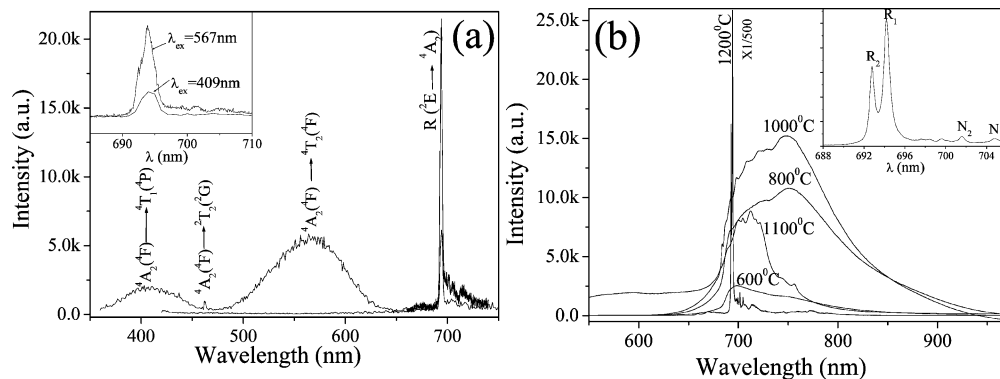

Figure 6. (a) Room temperature excitation (left) and emission (right) spectra for the Al$_2$O$_3$:Cr^{3+} nanotubes calcined at 1200 °C, measured with a xenon lamp as a light source; (b) room temperature PL spectra for Al$_2$O$_3$:Cr^{3+} nanotubes calcined at various temperatures, excited by the 514.5 nm line of an Ar$^+$ ion laser. The curve for the sample calcined at 1200 °C (in panel b) is divided by 500 for clarity comparison. The insets, corresponding to the spectra for the samples calcined at 1200 °C, are shown on an enlarged scale. Characteristic R$_1$ and R$_2$ lines of ruby crystal are observed peaking at 694.3 and 692.9 nm.

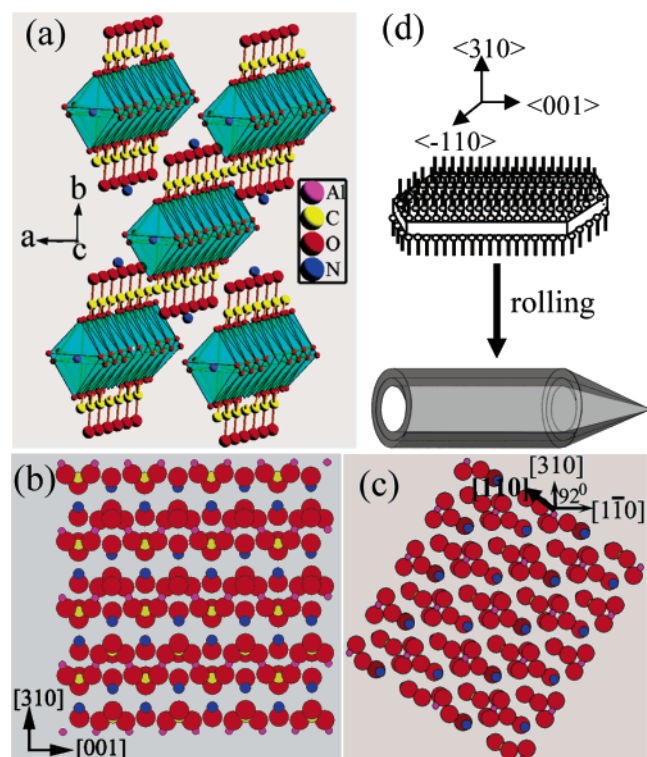Synthesis of Al₂O₃:Cr³⁺ Nanotubes

J. Phys. Chem. B, Vol. 110, No. 32, 2006 **15753**

Figure 7. (a) Three-dimensional sketch of $NH_4Al(OH)_2CO_3$ crystal structure. (b and c) Atomic projections along $[\bar{1}10]$ and $[001]$ directions, respectively. (d) Schematic formation illustration for the $NH_4Al(OH)_2CO_3$ nanotube growth from lamellar inorganic−surfactant structures to rolled-up nanotubes. Lamellar structures represent the $NH_4Al(OH)_2CO_3$ crystal nucleus, and the light dots in the surface correspond to the CTA^+ ions absorbed selectively on the $\pm(110)$ surface of the $NH_4Al(OH)_2CO_3$ crystal by hydrogen bonds.

of the growth can be understood by considering the structured properties of the $NH_4Al(OH)_2CO_3$ crystal. $NH_4Al(OH)_2CO_3$ can form a highly oriented small cluster as a nascent embryo with top/bottom surfaces of $\pm(110)$, and a triangle tip in growth direction of $\pm\langle001\rangle$ (chain axis). Under the electrostatic interaction of hydrogen bonding, highly concentrated CTA^+ ions can be adsorbed easily on the layered surface of $NH_4Al(OH)_2CO_3$ nuclei and form highly oriented lamellar inorganic−surfactant hybrid structures, resulting in a great decrease of the $\{110\}$ surface energy, which can inhibit effectively crystal growth in the directions perpendicular to $\{110\}$ facets and favor the anisotropic growth along their chain axis directions of $\langle001\rangle$, and the formation of laminar structures. In addition, the adsorption also results in a weakening of the interlayer bonds between negatively charged (AlO_6) layers, which facilitates the rolling and folding of layered crystallites into nanotubes.[5] From the crystal projections along $[\bar{1}10]$ and $[001]$ directions (Figure 7b,c), it can be seen that the atom arrangement on the upper

and lower $\{110\}$ planes is asymmetric; hence the adsorption of surfactant on the $\{110\}$ facets easily results in an asymmetrical strain. Moreover, in the crystallography (110) and $(\bar{1}10)$ are equivalent and their plane included angle is 122°. Because of the small difference in surface energy between (110) and $(\bar{1}10)$, a slight fluctuation can cause the crystal to grow from (110) to $(\bar{1}10)$. And thus, with the growth of the nascent embryo, the lamellar inorganic−surfactant hybrid structures with $\pm(110)$ surfaces are lost very easily along the $\pm[\bar{1}10]$ directions and result in a folding and coiling, which is of advantage to the minimum energy configuration due to the reduction of the surface area and the formation of chemical bonds. In the case of hydrothermal treatment, the urea can slowly hydrolyze in aqueous solutions to produce CO_3^{2-}, OH^-, and NH_4^+ ions, which can react with Al^{3+} and Cr^{3+} ions to form Cr^{3+}-doped $NH_4Al(OH)_2CO_3$ homogeneous precipitation. Such a slow reaction rate is closer to equilibrium reaction conditions and more favorable for the self-assembly process, retaining initial anisotropic nucleation of the crystal and subsequent gentler rolling action. As a result, the thermodynamically stable 1D tubular architectures with an axis of $\langle001\rangle$ and a wall of $\{110\}$ can be formed with the assistance of the CTAB surfactant soft-template. The schematic formation illustration is shown in Figure 7d. Through the reaction process the surfactant CTAB not only acts as a micelle, but importantly acts as structure-directing agent and stabilizer, controlling the morphology and structured orientation of the precipitate. If the layered structures are collapsed or the growth of the $\langle\bar{1}10\rangle$ direction is also impeded effectively at the initial growth stage, rodlike nanostructures growing along the $[001]$ direction would be formed. Due to the close ion radii and the same valence between Cr^{3+} (0.063 nm) and Al^{3+} (0.051 nm), Cr^{3+} ions with a low concentration can occupy substitutionally Al^{3+} sites in the lattice of $NH_4Al(OH)_2CO_3$ and form powder with a very slight reddish tint. Similarly, Cr^{3+} ions can also penetrate uniformly into the host lattice of Al_2O_3 and form substituted solid solution in the course of the subsequent heat treatment.

The interpretation can be verified on the basis of the TEM observation for $NH_4Al(OH)_2CO_3$ nanotubes. The SAED pattern of a relatively large nanotube with a diameter of about 500 nm, inset in Figure 8a, is taken and the electron beam is incident at the central region of the tube. It can only be indexed to a set of fundamental patterns of the $[310]$ zone axis. Because the angle between the $[310]$ direction and the normal of the (110) plane is only 2°, the surface vertical to the incident beam should be the (110) plane. As seen from the high-magnification TEM images (Figure 8b,c), the multilayered structure of the tube wall can be resoluble by alternate dark and bright contrasts; and moreover, quantities of stacking faults are parallel to the tube axis. In addition, nanosheets and needlelike nanotubes with a closed end, displayed respectively in Figure 8, panels d and e, can be also observed occasionally. It is due to the initial growth
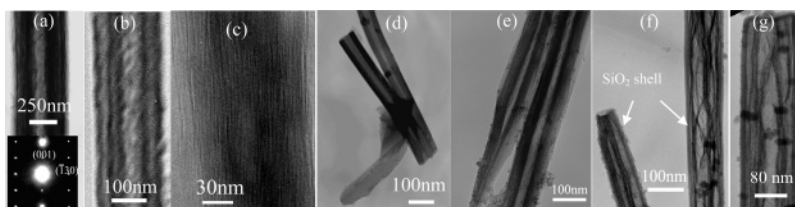

Figure 8. (a) TEM image of a nanotube with a diameter of about 500 nm; the corresponding SAED pattern was taken along the $[310]$ zone axis and the tube axis is perpendicular to the row of $\{001\}$ reflections. (b and c) High-magnification $NH_4Al(OH)_2CO_3$:Cr^{3+} nanotubes, showing the multilayered structure of the tube wall and quantities of stacking faults parallel to tube axis. (d) $NH_4Al(OH)_2CO_3$:Cr^{3+} nanotubes and nanosheets. (e) Needlelike $NH_4Al(OH)_2CO_3$:Cr^{3+} nanotube with a closed end. (f and g) Al_2O_3:Cr^{3+} nanotubes coated with SiO_2 shell after annealing at 500 °C, showing a multilayer separation of the inner Al_2O_3 nanotube wall.

Cheng et al.

of the NH₄Al(OH)₂CO₃ lamellar crystal along the [001] direction with a triangle tip that some needlelike nanotubes with a closed end exist in the samples after rolling-up. These features adequately indicate that the formation mechanism of NH₄Al-(OH)₂CO₃ nanotubes should come from the rolling action of layered materials under the assistance of a surfactant soft-template. To further confirm the fact and the structure of the multilayered tube wall, the NH₄Al(OH)₂CO₃ sample was coated with a thin SiO₂ shell and formed into double coaxial nanotubes by a sol−gel technique,[47] and then a heat treatment was conducted for the sample in air at 500 °C, as shown in Figure 8f,g. It can be seen that after heat treatment, the inner Al₂O₃ wall of the double coaxial nanotubes is separated into some thinner layers due to the formation of the stress from the decomposition and shrinkage of the precursors, distinctly confirming that the NH₄Al(OH)₂CO₃ tube walls consist of multilayer cylinders which are cohered by relatively weak interaction.

4. Conclusions

In summary, NH₄Al(OH)₂CO₃:Cr³⁺ nanotubes with high surface area, templated by surfactant assemblies, were successfully synthesized through a novel homogenization precipitation method and Al₂O₃:Cr³⁺ nanotubes with different crystalline phases were also obtained by postannealing the resulting precursors at various temperatures. The formation mechanism of NH₄Al(OH)₂CO₃:Cr³⁺ nanotubes should originate from the self-rolling action of the layered compound under the assistance of the surfactant soft-template. The simple synthetic procedure, excellent reproducibility, clean reactions, high yield, and fine quality of products in this work make the present route attractive and significant. This synthesis strategy can be easily extended to the synthesis of other kinds of polynary intricate nanomaterials by selecting an appropriate reaction and corresponding inorganic−surfactant hybrids. High specific surface area γ-Al₂O₃ and high crystalline α-Al₂O₃ with characteristic stimulated emission of the R₁ and R₂ line transitions of single ion Cr³⁺ in the octahedral sites of spinel block implies that aluminum oxide nanotubes could serve as light-emitting devices in nanosized optoelectronic applications doped with different elements and stable catalyst supports of metal clusters. On the basis of the uniquely hollow and fluorescent characteristics of individual nanotubes, the ruby nanostructures will offer interesting possibilities for novel laser applications with powdered media. In addition, these nanostructures might be suitable as a physical shield for the inserted biomolecules, biomolecule delivery, biolabeling, and biodetecting. Further work is underway to study other properties of this novel tubular morphology and the possibility of synthesizing other polynary complex nanotubes, and to build functional nanoscale devices based on the tubes.

References and Notes

(1) Xia, Y. N.; Yang, P. D.; Sun, Y. G.; Wu, Y. Y.; Mayers, B.; Gates, B.; Yin, Y. D.; Kim, F.; Yan, Y. Q. *Adv. Mater.* **2003**, *15*, 353.

(2) Wang, Z. L. *J. Phys.: Condens. Matter* **2004**. *16*, R829.

(3) Law, M.; Goldberger, J.; Yang, P. D. *Annu. Rev. Mater. Res.* **2004**, *34*, 83.

(4) Steinhart, M.; Wehrspohn, R. B.; Gösele, U.; Wendorff, J. H. *Angew. Chem.*, *Int. Ed.* **2004**, *43,* 1334.

(5) Patzke, G. R.; Krumeich, F.; Nesper, R. *Angew. Chem.*, *Int. Ed.* **2002**, *41*, 2446.

(6) Tian, Z. R.; Voigt, J. A.; Liu, J.; Mckenzie, B.; Xu, H. F. *J. Am. Chem. Soc.* **2003**, *125*, 12384.

(7) Wu, Q.; Hu, Z.; Wang, X. Z.; Lu, Y. N.; Chen, X.; Xu, H.; Chen, Y. *J. Am. Chem. Soc.* **2003**, *125*, 10176.

(8) Kim, H. J.; Lee, H. C.; Rhee, C. H.; Chung, S. H.; Lee, H. C.; Lee, K. H.; Lee, J. S. *J. Am. Chem. Soc.* **2003**, *125*, 13354.

(9) Nath, M.; Govindaraj, A.; Rao, C. N. R. *Adv. Mater.* **2001**, *13*, 283.

(10) Goldberger, J.; He, R. G.; Zhang, Y. F.; Lee, S.; Yan, H. Q.; Choi, H. J.; Yang, P. D. *Nature* **2003**, *422*, 599

(11) Hu, J. Q.; Bando, Y.; Golberg, D.; Liu, Q. L. *Angew. Chem.*, *Int. Ed.* **2003**, *42*, 3493.

(12) Yin, L. W.; Bando, Y.; Zhu, Y. C.; Golberg, D.; Li, M. S. *Appl. Phys. Lett.* **2004**, *84*, 3912.

(13) Hu, J. Q.; Bando, Y.; Liu, Z. W.; Zhan , J. H.; Golberg, D.; Sekiguchi, T. *Angew. Chem.*, *Int. Ed.* **2004**, *43*, 63.

(14) Hu, J. Q.; Bando, Y.; Zhan, J. H.; Liu, Z. W.; Golberg, D.; Ringer, S. P. *Adv. Mater.* **2005**, *17*, 975.

(15) Chen, C. C.; Liu, Y. C.; Wu, C. H.; Yeh, C. C.; Su, M. T.; Wu, Y. C. *Adv. Mater.* **2005**, *17*, 404.

(16) Dörre, E.; Hübner, H. *Alumina−Processing, Properties, and Applications*; Springer-Verlag: Berlin, Germany, 1984; p 216.

(17) Kim, Y.; Lee, S. M.; Park, C. S.; Lee, S. L.; Lee, M. Y. *Appl. Phys. Lett.* **1997**, *71*, 3604.

(18) Gusev, E. P.; Copel, M.; Cartier, E.; Baumvol, I. J. R.; Krug, C.; Gribelyuk, M. A. *Appl. Phys. Lett.* **2000**, *76*, 176.

(19) Pillonnet-Minardi, A.; Marty, O.; Bovier, C.; Garapon, C.; Mugnier, J. *Opt. Mater.* **2001**, *16*, 9.

(20) Moodera, J. S.; Kinder, L. R.; Wong, T. M.; Meservey, R. *Phys. Rev. Lett.* **1995**, *74*, 3273.

(21) Padture, N. P.; Gell, M.; Jordan, E. H. *Science* **2002**, *296*, 280.

(22) Gates, B. C. *Chem. Rev.* **1995**, *95*, 511.

(23) Bäumer, M.; Freund, H. J. *Prog. Surf. Sci.* **1999**, *61*, 127.

(24) Dellwig, T.; Rupprechter, G.; Unterhalt, H.; Freund, H. J. *Phys. Rev. Lett.* **2000**, *85*, 776.

(25) Morpeth, L. D.; McCallum, J. C. *Appl. Phys. Lett.* **2000**, *76*, 424.

(26) Peng, X. S.; Zhang, L. D.; Meng, G. W.; Wang, X. F.; Wang, Y. W.; Wang, C. Z.; Wu, G. S. *J. Phys. Chem. B* **2002**, *106*, 11163.

(27) Fang, X. S.; Ye, C. H.; Xu, X. X.; Xie, T.; Wu, Y. C.; Zhang, L. D. *J. Phys.: Condens. Matter* **2004**, *16*, 4157.

(28) Fang, X. S.; Ye, C. H.; Peng, X. S.; Wang, Y. H.; Wu, Y. C.; Zhang, L. D. *J. Mater. Chem.* **2003**, *13*, 3040.

(29) Zhu, H. Y.; Riches, J. D.; Barry, J. C. *Chem. Mater.* **2002**, *14*, 2086.

(30) Valcárcel, V.; Pérez, A.; Cyrklaff, M.; Guitián, F. *Adv. Mater.* **1998**, *10*, 1370.

(31) Yu, Z. Q.; Du, Y. W. *J. Mater. Res.* **1998**, *13*, 3017.

(32) Satishkumar, B. C.; Govindaraj, A.; Vogl, E. M.; Basumallick, L.; Rao, C. N. R. *J. Mater. Res.* **1997**, *12*, 604.

(33) Pu, L.; Bao, X.; Zou, J.; Feng, D. *Angew. Chem.*, *Int. Ed.* **2001**, *40*, 1490.

(34) Kuang, D. B.; Fang, Y. P.; Liu, H. Q.; Frommen, C.; Fenske, D. *J. Mater. Chem.* **2003**, *13*, 660.

(35) Hwang, J.; Min, B.; Lee, J. S.; Keem, K.; Cho, K.; Sung, M. Y.; Lee, M. S.; Kim, S. *Adv. Mater.* **2004**, *16*, 422.

(36) Xiao, Z. L.; Han, C. Y.; Welp, U.; Wang, H. H.; Kwok, W. K.; Willing, G. A.; Hiller, J. M.; Cook, R. E.; Miller, D. J.; Crabtree, G. W. *Nano Lett.* **2002**, *2*, 1293.

(37) Li, Y. B.; Bando, Y.; Golberg, D. *Adv. Mater.* **2005**,*17*, 1401.

(38) Jamison, S. P.; Imbusch, G. F. *J. Lumin.* **1997**, *75*, 143.

(39) Toyoda, T.; Obikawa, T.; Shigenari, T. *Mater. Sci. Eng. B* **1998**, *1/2*, 33.

(40) Cao, M. H.; Hu, C. W.; Wang, Y. H.; Guo, Y. H.; Guo, C. X.; Wang, E. B. *Chem. Commun.* **2003**, 1884.

(41) Li, Y.; Li, X.; Deng, Z. X.; Zhou, B.; Fan, S.; Wang, J.; Sun, X. *Angew. Chem.*, *Int. Ed.* **2002**, *41*, 333.

(42) Xiong, Y. J.; Xie, Y.; Li, Z. Q.; Li, X. X.; Gao, S. M. *Chem. Eur. J.* **2004**, *10*, 654.

(43) Sun, X. M.; Chen, X.; Deng, Z. X.; Li, Y. D. *Mater. Chem. Phys.* **2002**, *78*, 99.

(44) Xiong, Y. J.; Xie, Y.; Yang, J.; Zhang, R.; Wu, C. Z.; Du, G. A. *J. Mater. Chem.* **2002**, *12*, 3712.

(45) Zhang, L. Z.; Yu, J. C.; Mo, M. S.; Wu, L.; Kwong, K. W.; Li, Q. *Small* **2005**, *1*, 349.

(46) An appropriate amount of NH₄Al(OH)₂CO₃:Cr nanotubes was dispersed in 200 mL of 2-propanol by sonicating for more than 30 min. Deionized water (10m mL) and 28% ammonia (7.5 mL) were added. Finally, the right amount of tetraethyl orthosilicate was added into the mixture drop by drop. The mixture was then sonicated for about 2 h.